UNIVERSITY OF CALIFORNIA
RIVERSIDE

Phase Plate Enhanced Hyperspectral Imaging Using Visible-Light Optical Coherence Tomography (HSI-OCT) for Retina Imaging and Oximetry

A Thesis submitted in partial satisfaction
of the requirements for the degree of

Master of Science

in

Bioengineering

by

Jorge de Jesus Sanchez

December 2018

Thesis Committee:
Dr. B. Hyle Park, Chairperson
Dr. Joshua Morgan
Dr. William H. Grover

The Thesis of Jorge de Jesus Sanchez is approved:

_____

_____

_____

Committee Chairperson

University of California, Riverside

Table of Contents

Chapter 1: Background and Theory 1

1.1 Introduction to Optical Coherence Tomography 1

1.2 Spectral Domain OCT (SD-OCT) 4

1.3 Visible Light OCT 9

1.4 Phase Plate 15

Chapter 2: Hyperspectral Imaging Optical Coherence Tomography (HSI-OCT) for Retinal Imaging and Oximetry 19

2.1 Introduction 19

2.2 Materials and Methods 21

2.2.1 Wavelength Filters 21

2.2.2 Preparation of Phase Plate 21

2.2.3 In Vitro Blood Sample Preparation 23

2.2.4 System Specifications 23

2.2.4 OCT Data Acquisition and Processing 25

2.2.5 Spectroscopic Processing 26

2.2.6 Statistical Analysis 26

2.3 Results and Discussion 26

2.3.1 Phase Plate 26

2.3.2 Dichroic Wavelength Filters 27

2.3.3 In Vitro Spectroscopic Processing 28

2.4 Conclusion 32

References 33

List of Figures

Figure 1. Setup of a Michelson interferometer. The interferometer consists of a laser source, a beam splitter (B), two mirrors (M1 and M2), and a detector. The distances of the mirrors (L1 and L2) are of equal distance. By changing L2 it is possible to see different interferometric patterns. 2
Figure 2. Schematic of a classical TD-OCT system. It is composed of a low coherence light source, a reference arm, a as sample arm, and a detector. 3
Figure 3. a. Detected signal at the line scan camera along with the mathematical representation. b. Inverse Fourier transform of the detected signal along with its mathematical representation. The inverse Fourier transform can allow for us to get depth encoded structural information. 8
Figure 4. Fiber Based schematic of the HS-OCT system. The initial light beam from the super continuum source goes through DBS to filter out and separate the broad band light into two beams of visible light and NIR light. Visible light is then coupled into a 90/10 FS via a C. 90% of the visible light then goes to the reference arm and the remaining 10% goes to the sample arm. The light going to the sample goes through a C, then goes to a 2D galvanometer to achieve a raster scan. Light is focused onto the sample via two 100mm AR-L. The backscattered light travels back and is separated again via the DBS. Then the light beam first enters the spectrometer via a custom-made C and then enters a grating that separates the visible light into individual wavelengths. The separated light is then focused onto a LSC via a L. 11
Figure 5. A visual representation of the STFT. In a, the blue oscillations represent an interferogram and the underlying orange curve is the spectra that we wish to extract. b shows the Fourier transform of half of the signal on a logarithmic scale. C shows the window that is will be used. D is the convolution of the sample Fourier transform of our signal with the Gaussian window. E shows the demodulation, ie making the carrier frequency 0. Then f, the IFT of the demodulated data. We can see that the extracted spectrum is identical to that of the one in figure 5a. 15
Figure 6.Visual representation of a phase plate. It should be noted that the phase delay is introduced by the difference in the index of refraction between the phase plate material and air. 16
Figure 7. A visual representation of the STFT with a phase plate. In a, the blue oscillations represent an two interferograms that result from the phase. B shows the Fourier transform of half of the signal on a logarithmic scale in which two peaks appear that corresponding to the two phases. C shows the windows that is will be used. D is the convolution of the sample Fourier transform of our signal with the Gaussian windows. E shows the demodulation, ie making the carrier frequencies 0. Then f, the IFT of the demodulated data. We can see that the extracted spectra are identical to that of the one in figure 5a, by averaging these two we can get a better representation of the original spectrum. 18

Figure 8. OCT image of a retina that is in the late stages of diabetic retinopathy taken from the NIH website. As we can see, the layers of the retina are detached. 19
Figure 9. On the left is the 3mm polycarbonate phase plate that was made in our lab. The pinhole in the center was drilled with a 0.9mm drill bit. The resulting phase plate was put into a 5 axis kinematic base that is shown on the right. 22
Figure 10. Top left shows the spectrum that we have at our spectrometer. It is centered at about 580nm and has a bandwidth of 100nm. The top middle shows the roll-off of the system that was used and was found to be 3dB/mm. The top right figure shows the sensitivity of the system with an incident power of 0.240mW in the sample arm that was attenuated by 60dB. After subtracting the noise floor from the peak height, the resulting SNR was 93.94dB. The bottom left figure shows an axial resolution of about 5.87μm as determined by the FWHM of the PSF. The bottom middle figure shows a lateral resolution of 12.4μm as determined with an air force target. 24
Figure 11. The right figure shows the two peaks that resulted from placeing a silver mirror in the sample arm. The two peaks are at 1.70mm apart and of equal height. The left figure shows an intensity image of the right figure. 27
Figure 12. Resulting spectra that were extracted after using the wavelength filters. The blue spectra are the spectra that were obtained by placing the wavelngth filters in the sample arm and completely closing the reference arm. The orange spectra are the spectra that we extracted using our STFT processing method. 28
Figure 13. Spectra obtained with the spectrophotometer. The left shows the two characteristic peaks of oxy hemoglobin. The middle shows the characteristic peak of deoxy hemoglobin. The right shows the two oxy and deoxy curves superimposed and shows the isosbestic points that are also seen in literature. 30
Figure 14. Left figure shows the nominal deoxy and oxy spectra. The middle figure shows the spectra that we extracted using our processing method. The right figure shows the spectra that we extracted using the phase plate. 31
Figure 15. The top figures show the spectra that we extracted with (right) and without (left) the phase plate superimposed on the nominal data. The bottom figures show the same data but zoomed in to magnify the isosbestic point at 573nm in the black circle. 31

Chapter 1: Background and Theory

1.1 Introduction to Optical Coherence Tomography

Optical coherence tomography (OCT) is a diverse imaging modality that has been used to image the retina and diagnose various eye related disease due to its high resolution, fast acquisition speeds, and non-invasive properties [1] [2] [3] [4]. OCT has been increasingly used in a clinical setting since it was first introduced in 1991 [2] [5]; since that time, OCT has been able to improve how we diagnose and view eye maladies such as macular holes and macular pucker [5] [6], macular edema [7], age related macular degeneration [8], glaucoma [9], vitreous traction [10], and diabetic retinopathy (DR) [11].

Throughout the years, OCT as an imaging modality has undergone various iterations including time-domain OCT (TD-OCT), spectral domain OCT (SD-OCT), and swept source OCT (SS-OCT). By using low coherence interferometry, OCT can extract structural information from the surfaces and sub-surfaces of samples via backscattered light to generate depth resolved tomographic images. Although these imaging modalities slightly differ, the fundamental principle regarding how they obtain micron-scale resolution images remains the same. All iterations of OCT are based on a Michelson interferometer that uses low coherence interferometry shown in Figure 1. Low coherence interferometry allows us to measure the magnitude and time delay of optical echoes with extremely high sensitivity. This is achieved by the following. A beam of light from the source is shined onto a beam splitter that separates the light intensity

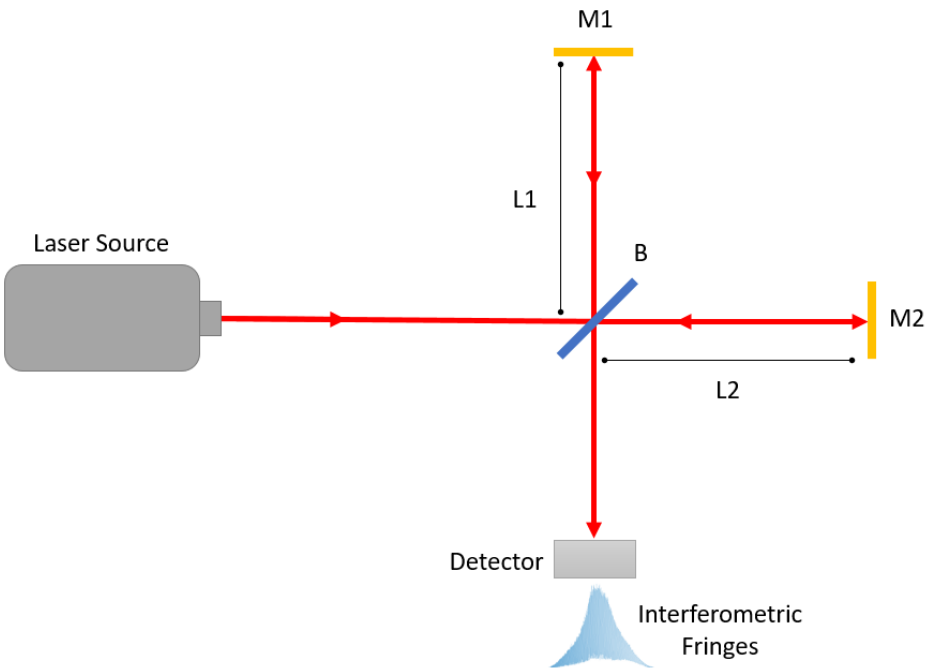

Figure 1. Setup of a Michelson interferometer. The interferometer consists of a laser source, a beam splitter (B), two mirrors (M1 and M2), and a detector. The distances of the mirrors (L1 and L2) are of equal distance. By changing L2 it is possible to see different interferometric patterns.

50/50 onto two separate mirrors that are spaced at equal distances (M1 and M2) from the beam splitter. Then, light from the mirrors is reflected back and recombined at the beam splitter. These two back reflected light beams can then be compared quantitatively by measuring the interference between the light two beams. The wave interference will be strong if the difference in path length between M1 and M2 is less than the coherence length. Coherence length is the propagation distance at which a coherent light wave maintains a specific degree of coherence. By varying the distance of one of the mirrors we can vary the interferometric fringes. The distance between fringes can then be quantified to get a precise measurement of the distance the mirror moved since the mirror is being moved by a reference point (M1). In order to see these interferometric

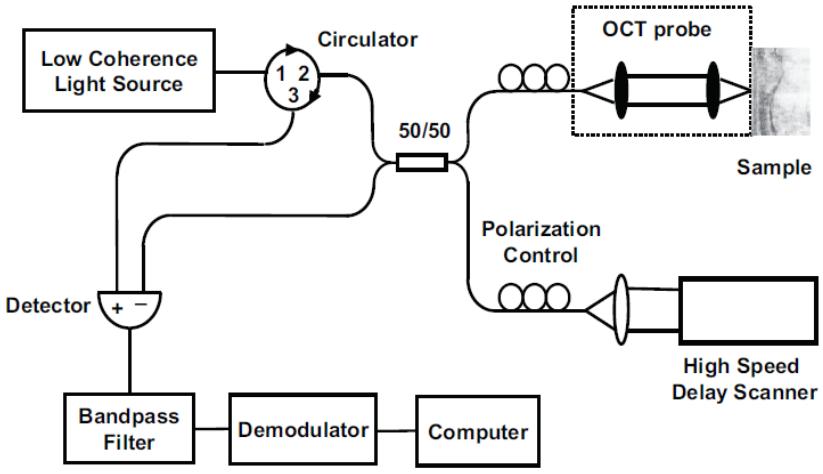

Figure 2. Schematic of a classical TD-OCT system. It is composed of a low coherence light source, a reference arm, a as sample arm, and a detector.

fringes over a short length with high axial resolution, the coherence length must be short. Furthermore, since coherence length is inversely proportional to the coherence length, a broad band light source must be used in OCT.

In essence, OCT is analogous to imaging using ultrasonic pulse-echo imaging (ultrasound imaging). Ultrasonic images are created by interpreting the back reflected echoes to obtain depth resolved information. OCT also produces a two-dimensional image using the backscattered light from some a sample, much like ultrasound [12]. However, OCT differs from ultrasonic pulse-echo imaging in that it using light as the carrier and requires a reference point due to light traveling at a much faster speed ($3x10^8$m/s) than sound (343m/s).

OCT is able to scan one depth profile scan (A-scan) within a few microseconds. This fast scanning rate is advantageous in that it greatly reduces the measured change of metabolic activity over time. Thus, OCT makes three-dimensional volumetric imaging possible.

1.2 Spectral Domain OCT (SD-OCT)

In TD-OCT (Figure 2) low coherence light is sent out from the source and split into two beams via a beam splitter. The two light beams propagate along two arms; the reference arm and the sample arm. Light from the sample arm is back scattered from different layers of some sample. Light in the reference arm is reflected from a mirror and travels a known distance. Both light beams then travel along the same path distance and interfere as they meet at the beam splitter. Interference between the two beams is only seen when their optical path lengths of the reference and sample arm are within the coherence length. By varying the path length of the mirror in the reference arm over a set distance using a high-speed delay scanner, we can image the corresponding depths of the sample. However, due to this scanning in the reference arm, TD-OCT produces coherent noise at all wavelengths. Thus, the speed at which TD-OCT can acquire images limited by having a low signal-to-noise ratio (SNR).

To overcome this limitation the interference spectrum can be detected in the Fourier Domain [13]. By placing a spectrometer in the detection arm, we can keep the reference arm at a fixed distance and view the backscattered echoes of light simultaneously, as a spectrum. So, instead of equating the optical path lengths of the reference and sample arm for different depths of the sample, we can record a Fourier transform of the spectrally resolved interference fringes. These spectrally resolved interferometric fringes come in the form of a spectrum that is split up by the spectrometer. We can then reconstruct the depth profile by performing the inverse Fourier transform via computer processing. This

eliminates the need of a high speed delay scanner, thus eliminating coherent noise and enhancing the systems overall SNR, while also acquiring data at a rapid speed.

The incident light in a Michaelson interferometer is considered a polychromatic plane wave [13] and its electric field can be expressed as Eq. 1.1

$$E_i = s(k,\omega)e^{i(kz-\omega t)} \tag{1.1}$$

where $s(k,\omega)$ is the electric field magnitude as a function of wavenumber k and the angular frequency ω. The wavenumber (k) is the spatial frequency of a wave, which is defined as $k = 2\pi/\lambda$, where λ is the wavelength. The angular frequency is defined as $\omega = 2\pi\nu$, where ν is the frequency of the wave. The optical path length along which the light is propagating is denoted as z and the time it takes is denoted as t. For N discrete reflectors from the sample, the electric fields of the reflected beams of light from the reference and sample arms can be expressed as Eq. 1.2 and Eq. 1.3

$$E_R = \frac{E_i}{\sqrt{2}} r_R e^{i(2kz_R)} = \frac{s(k,\omega)}{\sqrt{2}}\sqrt{R_R}e^{i(2kz_r-\omega t)} \tag{1.2}$$

$$E_S = \frac{E_i}{\sqrt{2}}\sum_{n=1}^{N} r_{Sn}e^{i(2kz_S)} = \frac{s(k,\omega)}{\sqrt{2}}\sum_{n=1}^{N}\sqrt{R_S}e^{i(2kz_S-\omega t)} \tag{1.3}$$

where r_R and r_S are the reflectivity of the reference arm mirror and of the n-th ($1 \leq n \leq N$) reflector of the sample, respectively. The intensity of the reflected optical waves are then detected by a photocurrent detector. The intensity of the photocurrent is proportional to Eq. 1.4

$$I(k,\omega) = \frac{\rho}{2}(E_R + E_S)^2 \tag{1.4}$$

where ρ is the sensitivity of the detector. Accordingly, we can ignore the angular frequency (ω) [13] and by using Euler's rule to simplify we end up with Eq. 1.5.

$$\begin{aligned} I(k) = \frac{\rho}{4}\left[S(k)\left(R_R + \sum_{n=1}^{N} R_{Sn}\right)\right] \\ + \frac{\rho}{2}\left[S(k)\sum_{n=1}^{N}\sqrt{R_R R_{Sn}}\cos[2k(z_R - z_{Sn})]\right] \\ + \frac{\rho}{4}\left[S(k)\sum_{n\neq m=1}^{N}\sqrt{R_{Sn}R_{Sm}}\cos[2k(z_{Sn} - z_{Sm})]\right] \end{aligned} \tag{1.5}$$

Here S(k) = $\langle|s(k,\omega)|^2\rangle$ is substituted, which encodes the power spectral dependence of the light source. For our purposes, a Gaussian shaped light source spectrum is convenient to use in modeling OCT since it approximates the shape of an actual light source and has a useful Fourier transform properties [13]. Equation 1.5 is comprised of three terms. The first term is referred to as the "DC component" and is independent of the optical path length difference between the reference and sample arm. The DC terms arises from the offset to the detector current. The second component is referred to as the "cross-correlation term" and is dependent on the light-source wavenumber k and the optical path length difference between the reflectors of the reference and sample arms (z). This portion is what allows us to obtain the axial position of each reflector and is thus the most important part. The cross-correlation term is proportional to the square root of the reflectivity of the sample. The third term is referred to as the "autocorrelation" term and it arises from the interference in the reflectors from

within the sample. The effects of autocorrelation are seen as artifacts in OCT images. If we assume the sample is stationary, we can assume the auto correlation term to be a constant and thus Eq. 1.5 can be simplified and rewritten as Eq. 1.6.

$$I(k) = I_r(k) + 2\sqrt{I_r(k)I_s(k)}\sum_{n=1}^{N}\alpha_n \cos(kz_n) + I_s(k) \tag{1.6}$$

where $I_r(k)$ and $I_s(k)$ are the intensities of reflected light from the reference and sample arm respectively and corresponding DC terms and auto-correlation terms seen in Eq. 1.5. It should be noted that they are independent of the axial position z and only a function of the wavenumber, k. α_n represents the square root of the sample reflectivity at depth z_n. The axial depth information, ie the cross-correlation terms are simplified as seen in the second term on the right hand side of equation 1.6.

The signal that is detected by the line scan camera is the spectrum in the Fourier domain. In order to obtain the depth information from this spectrum we must perform an inverse Fourier Transform (IFT). By taking the IFT of Eq. 1.6 we can obtain the depth information of a single scan at different depth positions. These depth positions indicate different light traveling times. To solve the IFT of Eq. 1.6 the following three Fourier transform pairs are used.

1 $$\cos(kz_n) \overset{F}{\Leftrightarrow} \frac{1}{2}[\delta(z - z_n) + \delta(z + z_n)]$$

2 $$1 \overset{F}{\Leftrightarrow} \delta(z)$$

3 $$\Upsilon(z) = e^{-z^2\Delta k^2} \overset{F}{\Leftrightarrow} S(k) = \frac{1}{\Delta k\sqrt{\pi}} e^{-\left[\frac{(k-k_0)}{\Delta k}\right]^2}$$

Based on the linearity property and convolution theorem of the Fourier Transform, $x(z) \otimes y(z) \overset{F}{\leftrightarrow} X(k)Y(k)$, the IFT of Eq. 1.6 can be written as Eq. 1.7:

$$\mathcal{F}^{-1}[I(k)] = i(z) = \frac{\rho}{8}\left[\Upsilon(z)\left(R_R + \sum_{n=1}^{N} R_{Sn}\right)\right] + \frac{\rho}{4}\left[\Upsilon(z) \otimes \sum_{n=1}^{N} \sqrt{R_R R_{Sn}}\, \delta[z \pm 2(z_R - z_{Sn})]\right] + \frac{\rho}{8}\left[\Upsilon(z) \otimes \sum_{n\neq m=1}^{N} \sqrt{R_{Sn} R_{Sm}}\, \delta[z \pm 2(z_{Sn} - z_{Sm})]\right] \quad 1.7$$

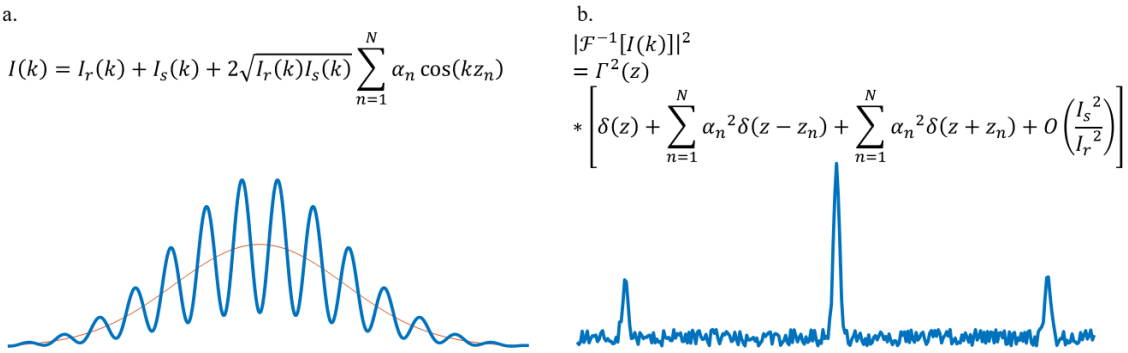

Figure 3. a. Detected signal at the line scan camera along with the mathematical representation. b. Inverse Fourier transform of the detected signal along with its mathematical representation. The inverse Fourier transform can allow for us to get depth encoded structural information.

where $\delta(\cdot)$ is the Dirac delta function. By taking advantage of the shifting properties of the Dirac delta function we can carry out the convolutions and obtain the interferometric measurement known as an A-scan shown in Eq 1.8

$$
\begin{aligned}
i(z) = \; & \frac{\rho}{8}\left[\Upsilon(z)\left(R_R + \sum_{n=1}^{N} R_{Sn}\right)\right] \\
& + \frac{\rho}{4}\left[\sum_{n=1}^{N}\left[\sqrt{R_R R_{Sn}}\,(\Upsilon[2(z_R - z_{Sn})] + \Upsilon[-2(z_R - z_{Sn}))]\right]\right] \\
& + \frac{\rho}{8}\left[\sum_{n\neq m=1}^{N}\left[\sqrt{R_{Sn}R_{Sm}}\,\Upsilon[2(z_{Sn} - z_{Sm})]\right.\right. \\
& \left.\left. + \; \Upsilon[-2(z_{Sn} - z_{Sm})]\right]\right]
\end{aligned}
\tag{1.8}
$$

Eq. 1.8 represents the axial depth information which is the result of the convolution of the coherence function envelope ($\Upsilon(z)$) with the sum of the DC terms and the interference between light waves returning from the reference and sample arms. It should be noted that all of the terms are in the spatial domain as a function of the axial position, z. A visual representation can be seen in Figure 3.

1.3 Visible Light OCT

Traditionally, OCT uses near-infrared (NIR) light to obtain anatomical changes in the retina in vivo with excellent resolution. These structures can be differentiated from one another due to the distinct changes in the refractive indices of retinal structures [13]

[14]. However, studies have shown that anatomical changes in the retina alone are not the most efficient way to determine visual acuity in many eye diseases including diabetic retinopathy (DR) [1] [3] [15] [16] [17]. Many studies have also demonstrated that DR and other eye diseases can be better diagnosed by measuring metabolic processes, such as retinal oxygenation content in the various layers via microelectrode recordings [18] [19]. However, this form of oximetry is highly invasive and limited to small areas of the retina. Additionally, capillary oxygen saturation is known to be the location of the earliest vascular changes in DR.

Thus, there is a need to noninvasively measure spectroscopic information of these capillaries in order to obtain the earliest possible diagnosis. This is where visible light OCT (vis-OCT) can be utilized. The use of visible light allows for OCT to be able to retrieve unique spectroscopic signatures that backscatter from a biological sample. This is due to the fact that visible light is known to have much higher scattering coefficients in biological tissue than NIR light, thus by using vis-OCT we can increase the imaging contrast without having to sacrifice much imaging depth. Much like regular FD-OCT, the vis-FD-OCT system, Figure 4, has the same set up. It is composed a reference arm, a sample arm, and a spectrometer. The main difference between traditional OCT and vis OCT is the light source that is used. In NIR OCT a super-luminescent diode (SLD) source is normally used. However, SLD sources typically

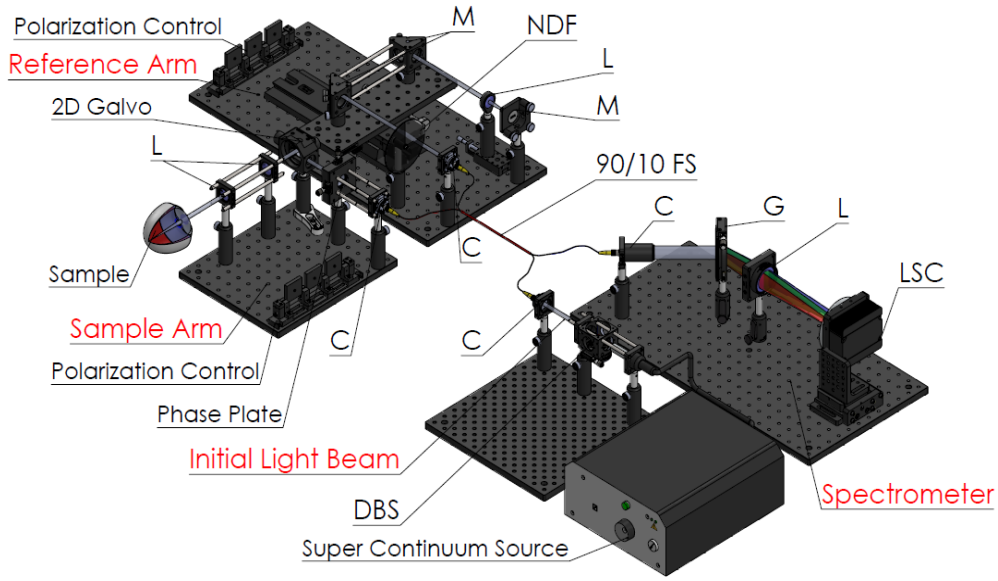

Figure 4. Fiber Based schematic of the HS-OCT system. The initial light beam from the super continuum source goes through DBS to filter out and separate the broad band light into two beams of visible light and NIR light. Visible light is then coupled into a 90/10 FS via a C. 90% of the visible light then goes to the reference arm and the remaining 10% goes to the sample arm. The light going to the sample goes through a C, then goes to a 2D galvanometer to achieve a raster scan. Light is focused onto the sample via two 100mm AR-L. The backscattered light travels back and is separated again via the DBS. Then the light beam first enters the spectrometer via a custom-made C and then enters a grating that separates the visible light into individual wavelengths. The separated light is then focused onto a LSC via a L.

operate in the wavelength range of 670 nm to 1600 nm. This range would not be ideal for visible light imaging since visible light spans from 400nm to 700 nm. Instead of an SLD, vis-OCT uses a supercontinuum (SC) source. These SC sources have a span from 400nm to 2500nm making them ideal for vis-OCT. It should be noted however, that SC sources have a much higher relative intensity noise (RIN) when compared to SLDs. This increased RIN noise reduces the sensitivity of the vis-OCT system when compared to traditional SLD operated OCT systems.

One of the biggest applications for vis-OCT is using it for spectroscopic analysis to quantify the oxygenated hemoglobin (HbO_2) and deoxygenated hemoglobin (Hb) in blood. The attenuation spectrum of blood is the weighted sum of the attenuation spectrum

fully oxygenated and deoxygenated blood which contains wither HbO_2 or Hb. So, by spectroscopically analyzing the OCT signal from some blood sample we can measure the oxygen saturation (sO_2) of said sample. Ultimately this could provide a picture of oxygen metabolism that occurs in the structure that is being imaged.

In order to obtain spectral information from a sample, two steps must be done. First, the wavelength dependent OCT signal intensities must be extracted from the raw data. Second, these intensities must then be fit the attenuation spectra of the known spectroscopic signatures of said sample. As previously stated, the detected interferogram in an OCT signal can be mathematically represented by Eq. 1.7 and its Fourier Transform by Eq. 1.9

$$I(k) = I_r(k) + 2\sqrt{I_r(k)I_s(k)}\sum_{n=1}^{N}\alpha_n \cos(kz_n) + I_s(k) \tag{1.9}$$

$$\begin{aligned}|\mathcal{F}^{-1}[I(k)]|^2 = \Gamma^2(z) \\ \otimes\left[\delta(z) + \sum_{n=1}^{N}{\alpha_n}^2\delta(z-z_n) + \sum_{n=1}^{N}{\alpha_n}^2\delta(z+z_n)\right. \\ \left. + O\left(\frac{{I_s}^2}{{I_r}^2}\right)\right]\end{aligned} \tag{1.10}$$

As previously mentioned, Γ(z) is the envelope of the autocorrelation function and α is the square root of the reflectivity of the sample arm at depth z and reference arm ($\sqrt{(R_R R_{Sn})}$). For a biological sample, the reflectivity at depth z, R_{Sn}, can be dependent on the wavenumber, which is affected by the backscattering spectrum (S_n) and the attenuation spectrum of the tissue above it [21].

In order to extract any valuable spectroscopic data, we must detect the variation in R_{Sn} with respect to the wavenumber. This can be done by applying a short time Fourier transform (STFT) to the interferogram I(k) to as seen in Eq. 1.10.

$$I_k(z, \tau_k) = STFT[I(k), w_k(\tau_k, \omega_k)] \quad (1.11)$$

where w_k is the window function used to extract the spectrum segment of interest and τ_k and ω_k are the center wavenumber and the bandwidth of the window function, respectively.

Alternatively, we can the STFT can also be applied to the reconstructed spatial domain signal, I(z) instead of the interferogram. In doing this we have Eq. 1.11 as follows:

$$I_z(z, \tau_z) = STFT[I(z), w_z(\tau_z, \omega_z)] \quad 1.12$$

where w_z is the windowing function that is used to select the region of interest along the axial direction, and τ_z and ω_z are the center position and the width of the window function respectively.

For example, Eq. 1.12 convolutes the interferogram I(k) of an OCT signal with a Gaussian window centered at τ and a width of ω. Once the two terms are convoluted it is crucial to remove the carrier frequency from the cross-correlation term of the equation by setting it z to zero, this process is known as a demodulation. By setting the carrier frequency to zero we can retrieve the underlying spectra in the original interferogram signal. Thus Eq. 1.12 can be rewritten as Eq. 1.13

$$I_k(z,\tau_k) = \left(I_r(k) + 2\sqrt{I_r(k)I_s(k)} \sum_{n=1}^{N} \alpha_n \cos(kz_n) + I_s(k) \right) \otimes \left(e^{-\frac{(z-\tau_k)}{\omega_z}} \right) \quad 1.13$$

$$I_k(z,\tau_k) = \left(I_r(k) + 2\sqrt{I_r(k)I_s(k)} \sum_{n=1}^{N} \sqrt{R_R R_{Sn}} + I_s(k) \right) \quad 1.14$$

Thus, Eq. 1.13 provides us with a number of spectra that are related to different depth ranges in the sample. A visual representation of this process is shown in Figure 5 for a single reflector. Figure 5a shows the detected signal at the line scan camera (Eq. 1.7). After taking the Fourier

transform we get Figure 5b. It should be noted that the strong peak is the carrier frequency and is responsible for the depth information. Then, we can use a Gaussian window (Figure 5c) centered at the strong peak of the Fourier transform. We can then convolve the Fourier Transform with the Gaussian window to get Figure 5d (Eq. 1.12). After this convolution a demodulation follows, Figure 5e and we make move the location of the peak to be zero. Once our signal is demodulated, we can take the Inverse Fourier Transform to obtain a spectrum as shown in Figure 5f and is mathematically represented by Eq. 1.13. For multiple reflectors, such as that from a biological signal, we can move the Gaussian

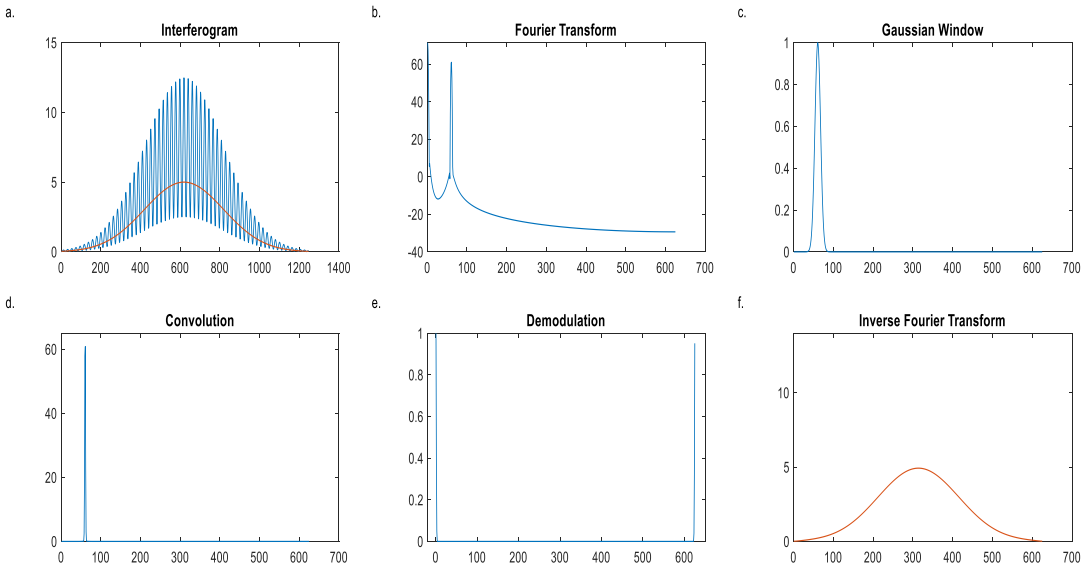

Figure 5. A visual representation of the STFT. In a, the blue oscillations represent an interferogram and the underlying orange curve is the spectra that we wish to extract. b shows the Fourier transform of half of the signal on a logarithmic scale. C shows the window that is will be used. D is the convolution of the sample Fourier transform of our signal with the Gaussian window. E shows the demodulation, ie making the carrier frequency 0. Then f, the IFT of the demodulated data. We can see that the extracted spectrum is identical to that of the one in figure 5a.

window across the Fourier transform as shown by the red arrow in Figure 5c. This would result in multiple spectra being extracted at different depths.

1.4 Phase Plate

Although the STFT and the demodulation work for extracting the underlying spectra of the incoming signal, some left over modulation remains.

In order to reduce this residual modulation, we propose using a custom-made phase plate. Using this phase-plate we can average out some of the modulation than would otherwise remain

Figure 6. Visual representation of a phase plate. It should be noted that the phase delay is introduced by the difference in the index of refraction between the phase plate material and air.

in the extrapolated spectra. Essentially, the use of an annular phase-plate will be used to separate light into different optical apertures that are encoded by a depth offset in an OCT A-Scan similar to that of Mo et al [20]. Using this phase plate allows us to acquire multiple OCT images in parallel in a single B scan. By averaging the spectra of the multiple images, we will ideally be able to remove some of the residual modulation. This will allow us to recover more accurate spectra in biological tissue. A visual representation of this can be seen in Figure 6. The left figure shows the phase plate of a thickness Δz and pin-hole in the middle with a diameter, f. The source of light (red beam on the left of phase plate) first encounters the phase plate. At this point, the portion of the beam that is hitting the phase plate will be delayed with respect to the center portion of the beam due to the fact that it travels through a longer optical path length. Thus, there is a phase delay between the two light beams. When the two beams encounter the sample that will be imaged, we will have two identical images that differ by a phase of Δz. Since the two images are identical and only differ by some phase, we can use both of the images to average out some of the residual noise that is left over after demodulation.

When the phase plate is inserted in the sample arm, there are three different paths for the sample light to reach the detector. The first light path is when the light travels

through the center of the phase-plate on the way to the sample and again through the center on its way to the detector. In the second path, the light the light passes through the phase plate on the way to the sample and then through the center on the way back to the detector. In the third path the light passes through the phase plate to the sample and back to the detector. These three path lengths give us three identical images that only vary by the depth at which they are located. Then, by using the STFT analysis that was previously described, we obtain the spectra of the three images that we obtained using the phase plate. These spectra should all be identical and should only differ by the known phase delay that we introduced. Thus, we can average the spectra together and reduce the residual modulation.

Moreover, the interference term for a single reflector with a phase plate can is given by:

$$I(k) = 2\sqrt{I_r(k)I_s(k)}\alpha\left\{\left[exp(i2kz) + exp\left(i2kz + ik\big(\Delta z(n-1)\big)\right)\ldots + exp\left(i2kz + ik2\big(\Delta z(n-1)\big)\right)\right] + C.C.\right\} \quad (1.15)$$

Which in turn can be written as the following:

$$I_{top}(k) = 2\sqrt{I_r(k)I_s(k)}\alpha exp(i2kz) \quad (1.16)$$

$$I_{middle}(k) = 2\sqrt{I_r(k)I_s(k)}\alpha\left(exp(i2kz)exp\big(ik\Delta z(n-1)\big)\right) \quad (1.17)$$

$$I_{bottom}(k) = 2\sqrt{I_r(k)I_s(k)}\alpha\left(exp(i2kz)exp\big(i2k\Delta z(n-1)\big)\right) \quad (1.18)$$

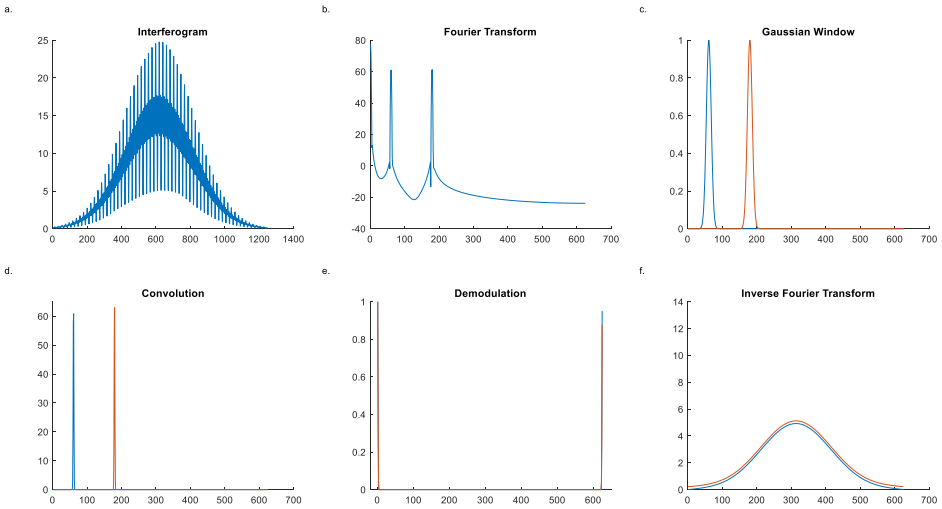

Figure 7. A visual representation of the STFT with a phase plate. In a, the blue oscillations represent an two interferograms that result from the phase. B shows the Fourier transform of half of the signal on a logarithmic scale in which two peaks appear that corresponding to the two phases. C shows the windows that is will be used. D is the convolution of the sample Fourier transform of our signal with the Gaussian windows. E shows the demodulation, ie making the carrier frequencies 0. Then f, the IFT of the demodulated data. We can see that the extracted spectra are identical to that of the one in figure 5a, by averaging these two we can get a better representation of the original spectrum.

where $\Delta z(n-1)$ is the optical path length difference between the center beam and the outer beam that was introduced by the phase plate. It is important to note here that Δz is the thickness of the phase plate and n is the refractive index of the phase plates material. Thus, we can obtain a total of three identical images that differ by some phase $\Delta z(n-1)$. A visual representation can be seen in Figure 7 along with the STFT and demodulation process. Note that only $I_{Top}(k)$ and $I_{middle}(k)$ are shown.

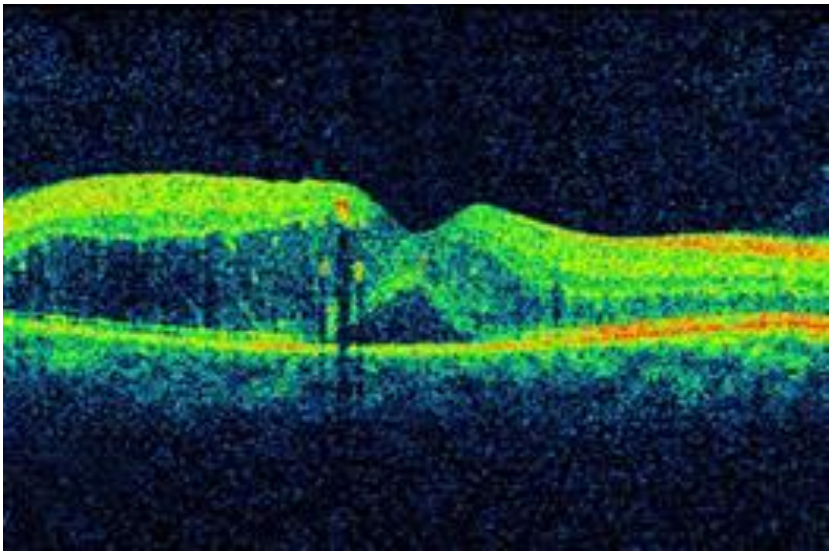

Figure 8. OCT image of a retina that is in the late stages of diabetic retinopathy taken from the NIH website. As we can see, the layers of the retina are detached.

Chapter 2: Hyperspectral Imaging Optical Coherence Tomography (HSI-OCT) for Retinal Imaging and Oximetry

2.1 Introduction

Ischemia and hypoxia have been shown to play critical roles in the pathophysiology of various diseases such as diabetic retinopathy (DR) [18] [19]. However, current diagnosis and treatments of said eye diseases focus primarily on late-stage vision loss that results from macular edema, macular ischemia, and neovascularization. Studies have suggested that retinal hypoxia could have a large role in DR, however there are no direct clinical measures of capillary hypoxia in humans [21] [22]. Furthermore, current research-based oximetry methods are only able to resolve large retinal blood vessels. These large blood vessels are usually not the location of preclinical vascular changes and thus should not be the focus of our attention. Thus, there is a lack of fundamental understanding about disease pathophysiology in humans, which

in turn limits the current treatments and our ability to develop therapies to treat early manifestations of these diseases. For example, the clinical course of DR occurs over 10-20 years, but current methods cannot detect the disease until there have been significant structural changes in the retina as seen in Figure 8 [23]. Therefore, researchers have hypothesized that a decrease of retinal capillary oxygen content (hypoxia) in human subjects with DR is an early biomarker of ischemic disease progression. Current hyperspectral oximetry methods can only resolve large retinal vessels due to the limitations in spatial and spectral range, resolution, image registration, and scattered light [24] [25]. Additionally, there is too much variability and late changes in large vessel oxygen, which suggests that it is not an ideal biomarker for early disease detection. Thus, there is a need for a non-invasive and clinically feasible method to detect retinal capillary hypoxia to better understand the pathophysiology of disease progression as well as to diagnose the diseases at a much earlier stage.

OCT provides excellent spatial resolution, is non-invasive, and has been used in a clinical setting for many years. Current OCT systems measure structural changes based on the reflectance intensity of the sample tissue using interferometry. Here we have designed and built a custom made broadband hyperspectral imaging OCT (HSI-OCT) machine that will allow for spectroscopic measurements of retinal tissue in vitro and in vivo on human and animal subjects. This HSI-OCT device will allow for us to measure the capillary oxygen content based on the spatially resolved spectroscopic signatures of oxygenated and deoxygenated hemoglobin. This device will allow for us to overcome the limitations in current oximetry systems and will allow for the early detection of metabolic

changes at the capillary level, which occur many years before current clinical changes are detectable, instead of the large vessel level. Essentially, this system will allow us to detect the earliest changes in metabolism in patients with retinal vascular disease. With the addition of a phase plate, we can also reduce the residual modulation and thus allowing us to better detect gradients of oxygen saturation between capillary regions with impaired flow and normal flow that may predict the future progression of the disease.

2.2 Materials and Methods

2.2.1 Wavelength Filters

In order to get a measure of how well we can recover differences in the extracted spectra with our method, we needed a static non-biological sample. So, we used a series of dichroic wavelength filters with various wavelengths transmission percentages at different central wavelengths and bandwidths. The following pairs of wavelength filter were used: 570nm-17nm-85% (PixelTeq), 570nm-20nm-95%T (PixelTeq), 575nm-17nm-90% (PixelTeq), 575nm-20nm-90%T (PixelTeq), 600nm-10nm-50%T (Thorlabs), 600-10nm-80%T (Edmund Optics), 600nm-80nm-75%(Edmund Optics), 600nm-40nm-75%(Thorlabs).

2.2.2 Preparation of Phase Plate

In order to reduce the residual modulation that is left over from the STFT, a custom-made phase plate was made. The phase-plate consists of a 3-mm thick polycarbonate round plate with a radius of 2.54cm. Then, a 0.5 mm drill bit was used to drill a hole in the center of the phase plate. This diameter was used to ensure that half of

Figure 9. On the left is the 3mm polycarbonate phase plate that was made in our lab. The pinhole in the center was drilled with a 0.9mm drill bit. The resulting phase plate was put into a 5 axis kinematic base that is shown on the right.

the light passed through the polycarbonate (with a phase delay), while the other half traveled through the air (without a phase delay). Given that the index of refraction of polycarbonate is 1.58, we have a phase delay of 1.74 mm. This number was chosen very carefully. For visible light OCT, we can achieve a penetration of depth of about 1.5-2.0 mm in tissue. Since we are using visible light, the penetration depth is lower than 2.0mm. Thus, by making our phase delay 1.74 mm we can ensure that the two resulting images are not overlapping with each other since the imaging depth is less than 1.75mm. The phase-plate was then inserted into a 5 axis micrometer to adjust the position of the phase plate to ensure the center of the incident beam was at exactly the center of the phase-plate (Figure 9).

2.2.3 In Vitro Blood Sample Preparation

Samples were prepared following the materials and methods of Karen et al. Whole heparinized porcine blood was obtained from the local farm at USC and all experiments were performed within 3 days after the blood was drawn. Sodium heparin was used as an anti-coagulant. Sodium dithionite (Sigma Aldrich) was used to fully deoxygenate the blood samples. The goal is to obtain the spectra of oxygenated hemoglobin and deoxygenated hemoglobin at 100 O_2% and 0 O_2%. By using a spectrophotometer (ThermoScientific Biomate 3S UV-VIS), we obtained a reference spectrum for oxy and deoxy hemoglobin. A total of 5 samples were measured. A total of 50μL f porcine blood was added to cuvettes followed by 2 mL of sodium phosphate buffer (PBS). PBS was added so that we had a blank as well as to dilute the blood samples. This experiment was done to compare the known spectra to those extracted from the HSI-OCT system with and without the phase plate as well as to verify that we have oxygenated and deoxygenated hemoglobin in the samples.

2.2.4 System Specifications

The HSI-OCT system used for our experiments was designed in our lab. Figure 4 shows a schematic of the SD-OCT system that was built. The entire fiber based optical system was mounted on 4 separate breadboards and inserted into a 19" server rack. A program made in Microsoft's Visual Studio along with National Instruments was used to acquire and view the data. Post image processing was done via Matlab r2018a.

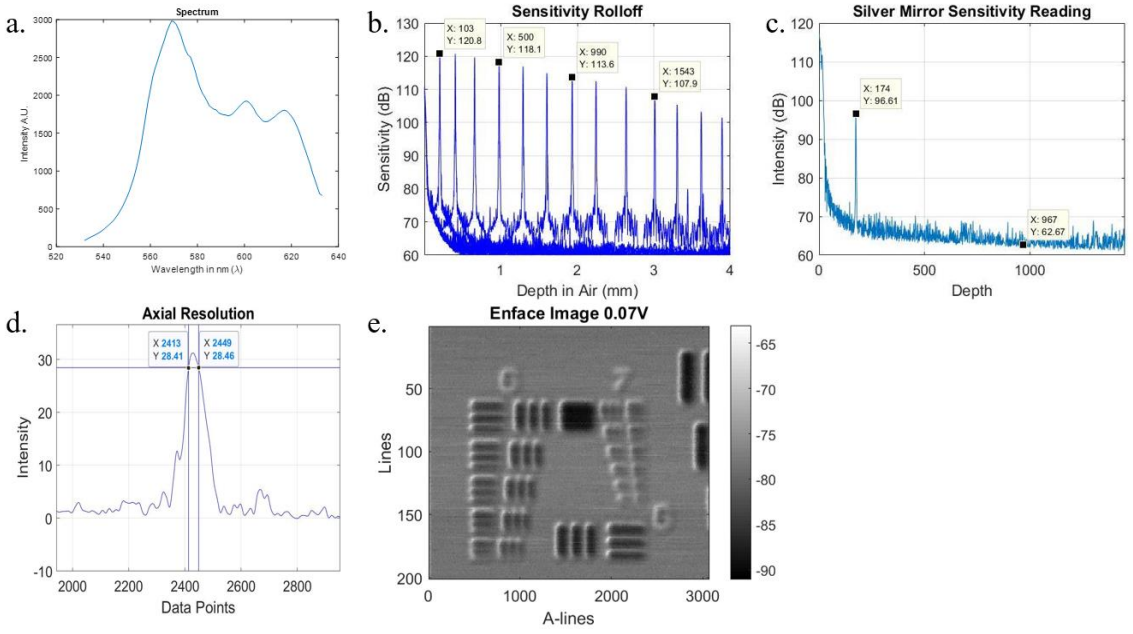

Figure 10. Top left shows the spectrum that we have at our spectrometer. It is centered at about 580nm and has a bandwidth of 100nm. The top middle shows the roll-off of the system that was used and was found to be 3dB/mm. The top right figure shows the sensitivity of the system with an incident power of 0.240mW in the sample arm that was attenuated by 60dB. After subtracting the noise floor from the peak height, the resulting SNR was 93.94dB. The bottom left figure shows an axial resolution of about 5.87µm as determined by the FWHM of the PSF. The bottom middle figure shows a lateral resolution of 12.4µm as determined with an air force target.

A broadband supercontinuum source was used as the light source that ranges from 300-2400nm. After filtering out wavelengths outside of the visible region using a dichroic filter, a bandwidth of 100nm was used that included wavelengths from 532nm to 633nm (Figure 10a). The system sensitivity and roll-off were characterized by placing a silver mirror (S-M) in the sample arm. In order to determine the wavelengths reaching our sample, two single wavelength filters (Chromas 532 and 633) were placed directly in front of the supercontinuum source beam path. Lateral resolution was determined using an Airforce target placed in the sample arm (figure 10e). Axial resolution was determined using the FWHM of the reflected image of silver mirror (figure 10d). The axial and lateral resolution of the system was 5.87µm and 12.4µm respectively. The signal to noise

ratio (SNR) of the system was determined by subtracting the noise floor from the peak height that was obtained from a single reflector in the Fourier domain that was attenuated by 60dB (Figure 10c) with an incident light of 0.240mW. The resulting SNR was 33.94dB. Thus, the sensitivity of the system was 93.94dB, which is on par with the amount needed to image biological tissue. The roll-off of the system was determined by changing the position of the reference arm mirror incrementally and was 3 dB/mm (Figure 10b), which is on par with other OCT systems.

It should be noted that 0.240mW incident light in the sample arm was specifically chosen. It was previously determined that this value was far below the maximum permissible light exposure on a human retina as determined by the Association of National Standards Institute (ANSI).

2.2.4 OCT Data Acquisition and Processing

Data was processed using a MATLAB and followed conventional reconstruction algorithms in SD-OCT [26]. Briefly, spectral resolution was determined by taking 1023 A lines for various light intensities at the sample arm with and without the phase plate. Light intensity was varied using an NDF and spectroscopic information was simulated by using a dichroic filter with selective absorption and reflection of the wavelengths in our range. The standard deviation and mean of 1023 A-lines per image were collected for twenty different light intensities. The resulting standard deviations and means were divided by each other and were plotted against the peak intensity of their respective images.

2.2.5 Spectroscopic Processing

All spectroscopic data was processed using Matlab R2018a. Our STFT method involved using a Gaussian window that spanned 70 points. This Gaussian window was convoluted with every point of the Fourier Transform of the interferogram that was obtained with the line scan camera. The resulting algorithm revealed the underlying spectra of sample that was being imaged. The spectra were then averaged together to obtain one spectrum that represented the reflection spectrum of the sample.

2.2.6 Statistical Analysis

In order to assess the precision of our method the resulting spectra that were obtained were compared to those obtained with the spectrophotometer. By doing the sum of the difference of squares between data, we can will be able to assess how well our method is when compared to not using a phase-plate.

2.3 Results and Discussion

2.3.1 Phase Plate

Using the phase plate that we fabricated in our lab we obtained the data in figure 11. We can see from the right figure that the two resulting peaks are spaced 1.74mm apart. It is also clear that the two peaks are close to the same height. The first image has a max intensity of 113.9 AU while the second peak has a height of 113.7AU. The left figure shows an intensity image of the right figure.

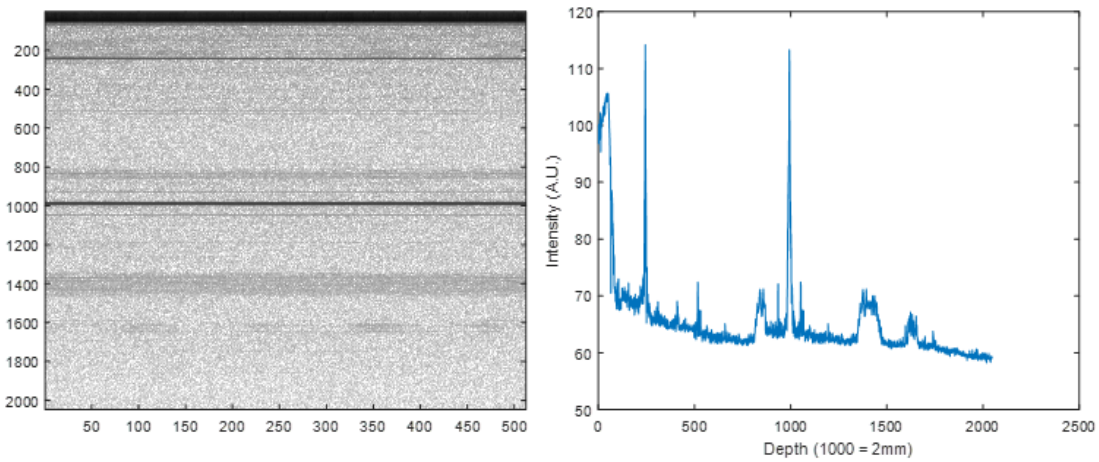

Figure 11. The right figure shows the two peaks that resulted from placeing a silver mirror in the sample arm. The two peaks are at 1.70mm apart and of equal height. The left figure shows an intensity image of the right figure.

2.3.2 Dichroic Wavelength Filters

The results of the dichroic wavelength filters are shown in figure 12. The blue curve represents the wavelength filter being placed in the sample are with the reference arm being attenuated by 100%. This gave us a reference-spectra so that we can see what the spectra looked like in our system. The orange curves represent the spectra that we extracted with our spectroscopic processing method. The two spectra were then superimposed onto one another to compare how well they compared and then side by side to see if there was a difference in intensity between the filters. We can see that for each filter the extracted spectra that we obtained with our processing method matches relatively well with that of the actual spctra. We can also see that the differences in heights of the wavelength filters are apparent and match that of the actual transmission percentages that were given with the wavelength filters.

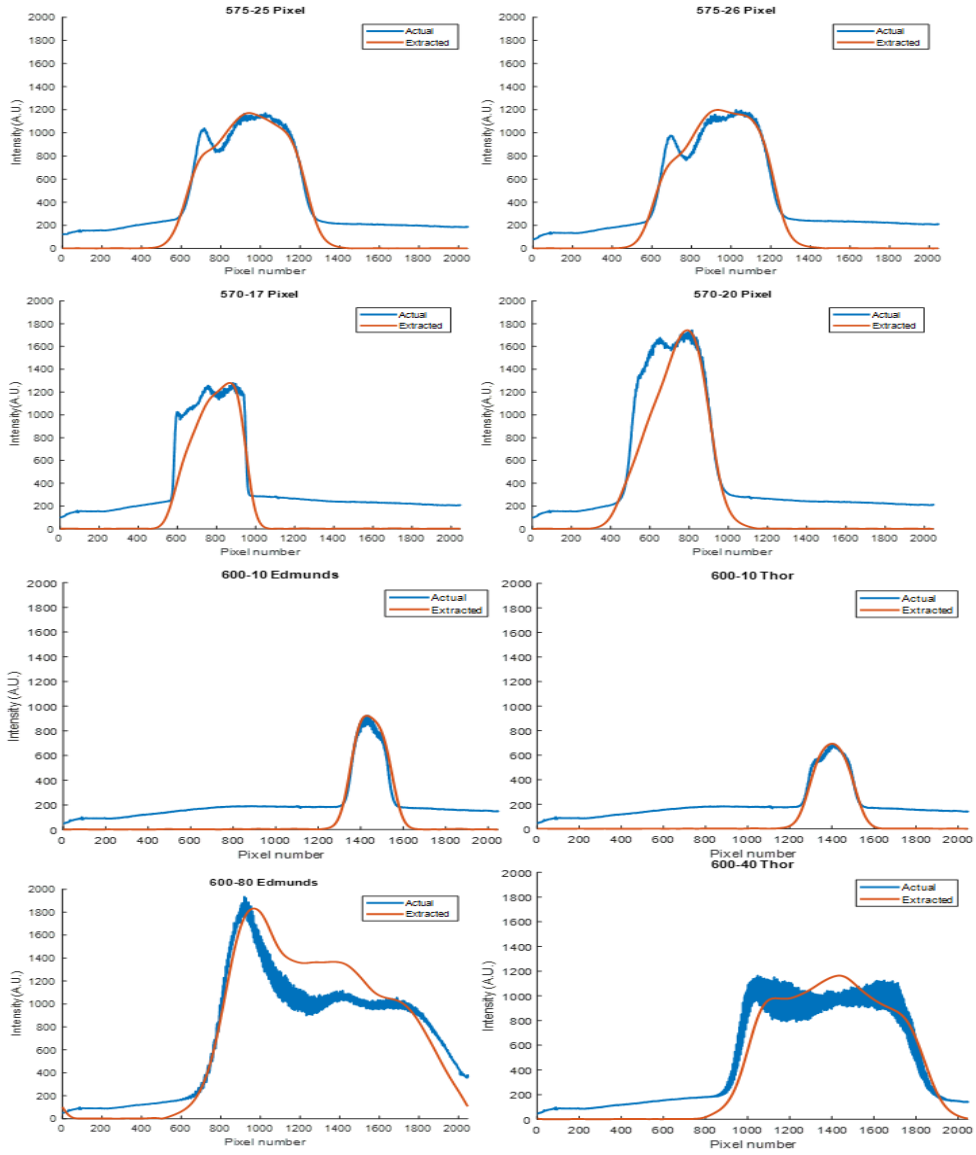

Figure 12. Resulting spectra that were extracted after using the wavelength filters. The blue spectra are the spectra that were obtained by placing the wavelngth filters in the sample arm and completely closing the reference arm. The orange spectra are the spectra that we extracted using our STFT processing method.

2.3.3 In Vitro Spectroscopic Processing

The resulting spectra that were obtained from the spectrophotometer are shown in Figure 13. The left figure shows all of the oxy measurements. It is clear that the most abundant species in the samples is oxygenated hemoglobin. We can see the characteristic

peaks that are seen in the absorption spectra of oxygenated hemoglobin at 530nm and 578nm. The middle figure shows the spectra for the samples once sodium dithionite was added to the samples. It is clear that this is the spectrum for the deoxy-hemoglobin. We can see the characteristic peak at 558nm for deoxy hemoglobin. The graph on the right shows the normalized spectra of oxy and deoxy samples superimposed onto each other. We can see that the isosbestic points that are seen in literature are also seen in our samples. Thus, we can conclude that our method for deoxygenating hemoglobin is valid so, we can use this to assess the validity of our HSI-OCT system.

Figure 14 shows the spectra that we obtained with our processing method and our HSI-OCT system with and without the phase plate. The middle figure shows the two spectra that we extracted without the phase plate and the figure on the farther left shows the spectra that we obtained with the phase plate. We can clearly differentiate the oxy and deoxy hemoglobin spectra from one another. Furthermore, we can see a peak at about 560nm for the deoxy-hemoglobin which was also seen in the spectrum that obtained from the spectrophotometer. Additionally, for the oxy-hemoglobin peak we can also see a peak at around 580nm which closely resembles one of the peaks we saw in the spectrophotometer data for oxy-hemoglobin. It should be clear to note that the second peak does not show up in our data because wavelengths from 550 and below cannot be seen in our system due to low intensity at the line scan camera of our HSI-OCT system.

If we look at the two sets of data, blood with and without the phase plate, it is apparent that the spectra that we obtained with the phase plate is smoother and has much less residual modulation than the data without the phase plate. From this we can see that

at any given wavelength we have a better representation of what the absorption was at that wavelength, than we would have if the phase plate was not there.

Furthermore, if we superimpose the phase plate and non-phase plate data on top of the data obtained from the spectrophotometer, figure 15 we can see how well the data compare to one another. If we look at the sum of squares for the phase plate and non-phase plate data, we can see get a value to measure how close the curves match to one another. The values for the deoxy with and without the phase plate are 0.6946 and 0.7660 respectively. The values for oxy with and without the phase plate are 0.6436 and 0.7477 respectively. Since we have lower values for the both the deoxy and oxy with the phase plate than without, it is safe to say that we have less variability in the data with the phase plate. Additionally, if we zoom into the data points in figure 15 in the black circle we can clearly see that the isosbestic point that we get from the phase plate data is much more apparent than without the phase plate.

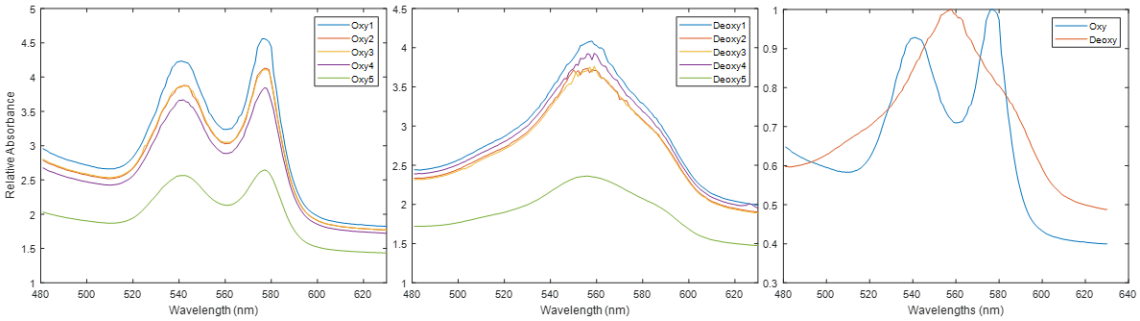

Figure 13. Spectra obtained with the spectrophotometer. The left shows the two characteristic peaks of oxy hemoglobin. The middle shows the characteristic peak of deoxy hemoglobin. The right shows the two oxy and deoxy curves superimposed and shows the isosbestic points that are also seen in literature.

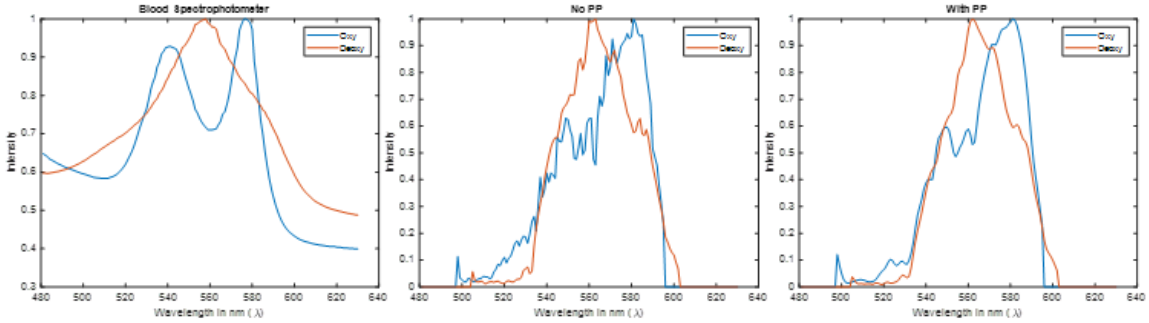

Figure 14. Left figure shows the nominal deoxy and oxy spectra. The middle figure shows the spectra that we extracted using our processing method. The right figure shows the spectra that we extracted using the phase plate.

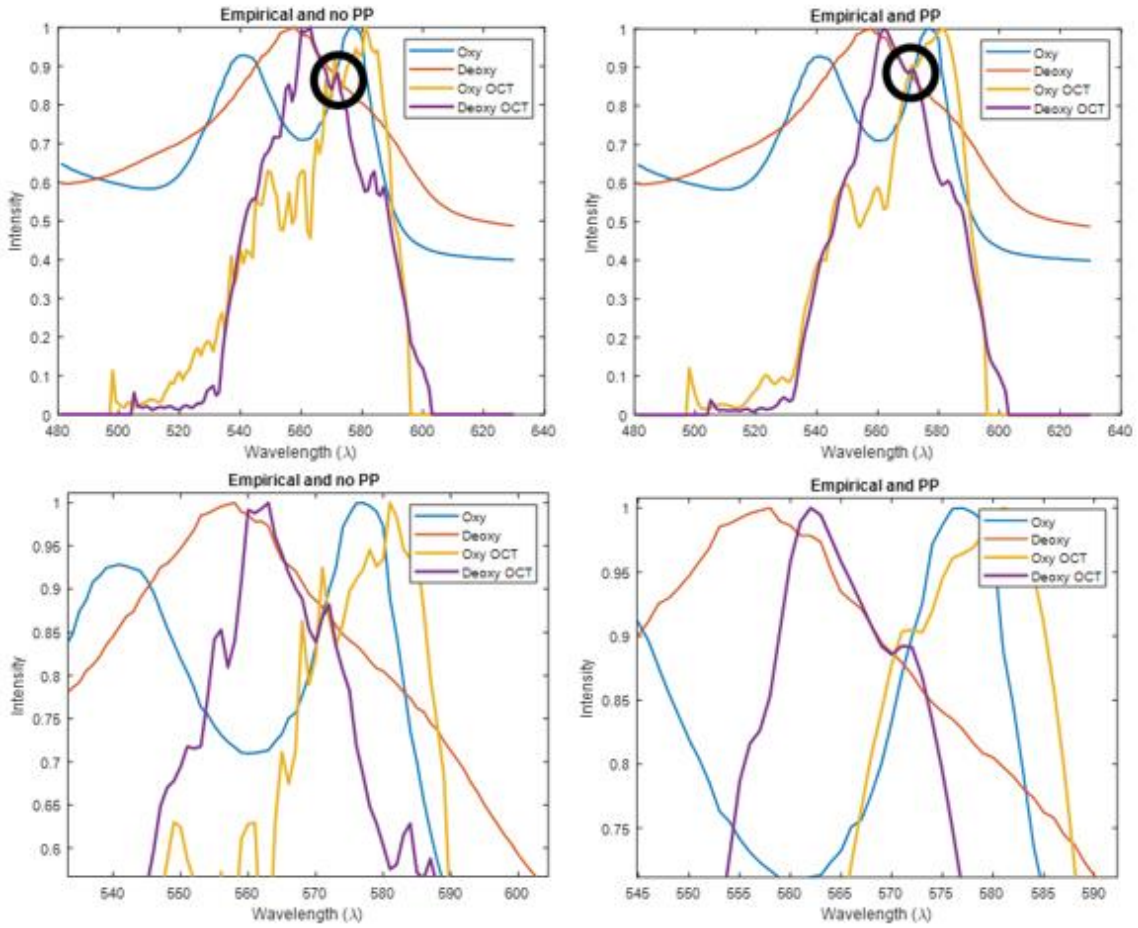

Figure 15. The top figures show the spectra that we extracted with (right) and without (left) the phase plate superimposed on the nominal data. The bottom figures show the same data but zoomed in to magnify the isosbestic point at 573nm in the black circle.

2.4 Conclusion

So, by looking the spectra that we obtained with our method we can safely say our method is valid for determining the difference between oxy and deoxy hemoglobin. Additionally, by looking at the sum of the difference of squares we can see that there us less variability in the extracted spectra when we use a phase plate than when we don't. From that we can conclude that using a phase plate improves our ability to extract oxy and deoxy spectra in vivo. Further improvements to the system must be done in order for the system to be used in vivo. Such improvements include using a better material for our phase plate. The phase plate that we used resulted in a loss of sensitivity. Additionally, there is significant chromatic aberration in the system which can be fixed by using an achromatized collimator.

References

[1] Amir H. Kashani, Ingrid E. Zimmer-Galler, Syed Mahmood Shah, Laurie Dustin, Diana V. Do, Dean Eliott, Julia A. Haller, Quan Dong Nguyen, "Retinal thickness analysis by race, gender, and age using Stratus OCT," *American Journal of Ophthalmology*, vol. 149, no. 3, pp. 496-502, 2010.

[2] Michelle L. Gabriele, Gadi Wollstein, Hiroshi Ishikawa, Larry Kagemann, "Optical Coherence Tomography: History, Current Status, and Laboratory Work," *Investigative Ophthalmology & Visual Science*, vol. 52, no. 5, pp. 2425-2436, 2011.

[3] Amir H. Kashani, Pearse A. Keane, Laurie Dustin, Alexander C. Walsh, Srinivas R. Sadda, "Quantitative subanalysis of cystoid spaces and outer nuclear layer using optical coherence tomography in age-related macular degeneration," *Investigative Ophthalmology & Visual Science*, vol. 50, no. 7, pp. 3366-3373, 2009.

[4] Francisco E. Robles, Christy Wilson, Gerald Grant, Adam Wax, "Molecular imaging true-colour spectroscopic optical coherence tomography," *Nature photonics*, vol. 5, no. 12, pp. 744-747, 2011.

[5] MichaelR. Hee, Carmen A. Puliafito, Carlton Wong, Jay S. Duker, Elias Reichel, Joel S. Schuman, Eric A. Swanson, James G. Fujimoto, "Optical Coherence Tomography of Macular Holes," *Ophthalmology*, vol. 102, no. 5, pp. 748-756, 1995.

[6] Jerry Sebag, Priya Gupta, Richard R. Rosen, Patricia Garcia, Alfredo A. Sadun , "Macular holes and macular pucker: the role of vitreoschisis as imaged by optical coherence tomography/scanning laser ophthalmoscopy," *Transactions of the American Ophthalmological Society*, vol. 105, pp. 121-131, 2007.

[7] Michael R. Hee, Carmen A. Puliafito, Carlton Wong, Jay S. Duker, Elias Reichel, Bryan Rutledge, Joel S. Schuman, Eric A. Swanson, James G. Fujimoto, "Quantitative Assessment of Macular Edema With Optical Coherence Tomography," *Archives of Ophthalmology*, vol. 113, no. 8, pp. 1019-1029, 1995.

[8] Michael R. Hee, Caroline R. Baumal, Carmen A. Puliafito, Jay S. Duker, Elias Reichel, Jason R. Wilkins, Jeffery G. Coker, Joel S. Schuman, Eric A. Swanson, James G. Fujimoto, "Optical Coherence Tomography of Age-related Macular Degeneration and Choroidal Neovascularization," *Ophthalmology*, vol. 103, no. 8, pp. 1260-1270, 1996.

[9] Joel S. Schuman, Michael R. Hee, Carmen A. Puliafito, Carlton Wong, Tamar Pedut-Kloizman, Charles P. Lin, Ellen Hertzmark, Joseph A. Izatt, Eric A. Swanson, James G. Fujimoto, "Quantification of Nerve Fiber Layer Thickness in Normal and Glaucomatous Eyes Using Optical Coherence Tomography: A Pilot Study," *Archives of ophthalmology,* vol. 113, no. 5, pp. 586-596, 1995.

[10] Hideki Koizumi, Richard F. Spaide, Yale L. Fisher, K Bailey Freund, James M. Klancnik Jr, Lawrence A. Yannuzzi, "Three-dimensional evaluation of vitreomacular traction and epiretinal membrane using spectral-domain optical coherence tomography," *American Journal of Ophthalmology,* vol. 145, no. 3, pp. 509-517, 2008.

[11] Massin P, Erginay A, Haouchine B, Mehid, A Ben, Paques M, Gaudric A, "Retinal thickness in healthy and diabetic subjects measured using optical coherence tomography mapping software," *European Journal of Ophthalmology,* vol. 12, no. 2, pp. 102-108, 2002.

[12] David Huang, Eric A. Swanson, Charles P. Lin, Joel S. Schuman, William G. Stinson, Warren Chang, Michael R. Hee, Thomas Flotte, Kenton Gregory, Carmen A. Puliafito, James G. Fujimoto, "Optical coherence tomography," *Science,* vol. 254, no. 5035, pp. 1178-1181, 1991.

[13] Michael Pircher, Robert J. Zawadzki,, "Review of adaptive optics OCT (AO-OCT): principles and applications for retinal imaging [Invited]," *Biomedical Optics Express,* vol. 8, no. 5, pp. 2536-2562, 2017.

[14] Mehreen Adhi, Jay S. Duker, "Optical coherence tomography – current and future applications," *Current opinion in ophthalmology,* vol. 24, no. 3, pp. 213-221, 2013.

[15] Bressler, Neil M; Edwards, Allison R; Antoszyk, Andrew N; Beck, Roy W; Browning, David J; Ciardella, Antonio P; Danis, Ronald P; Elman, Michael J; Friedman, Scott M; Glassman, Adam R; Gross, Jeffrey G; Li, Helen K; Murtha, Timothy J; Stone, Thomas W; Sun,, "Retinal thickness on Stratus optical coherence tomography in people with diabetes and minimal or no diabetic retinopathy," *American Journal of Ophthalmology,* vol. 145, no. 5, pp. 894-901, 2008.

[16] Hortensia Sánchez-Tocino, Aurora Alvarez-Vidal, Miguel J. Maldonado, Javier Moreno-Montañés, Alfredo García-Layana, "Retinal thickness study with optical coherence tomography in patients with diabetes," *Investigative Ophthalmology & Visual Science,* vol. 43, no. 5, pp. 1588-1594, 2002.

[17] Nunes S, Pereira I, Santos A, Bernardes R, Cunha-Vaz J., "Central retinal thickness measured with HD-OCT shows a weak correlation with visual acuity in eyes with CSME," *The British Journal of Ophthalmology,* vol. 94, no. 9, pp. 1201-1204, 2010.

[18] Constantin J. Pournaras,, Elisabeth Rungger-Brandle, Charles E. Riva, Sveinn H. Hardarson, Einar Stefansson, "Regulation of retinal blood flow in health and disease," *Progress in Retinal and Eye Research,* vol. 27, no. 3, pp. 284-330, 2008.

[19] Norbert D. Wangsa-Wirawan, Robert A. Linsenmeier, "Retinal Oxygen: Fundamental and clinical aspects," *Archives of Ophthalmology,* vol. 121, no. 4, pp. 547-557, 2003.

[20] Mo, Jianhu a., Mattijs de Groot, and Johannes F. de Boer, "Focus-Extension by Depth-Encoded Synthetic Aperture in Optical Coherence Tomography," *Optics Express,* vol. 21, no. 8, p. 10048–10061, 2013.

[21] Nguyen, Quan Dong, Syed Mahmood Shah, Elizabeth Van Anden, Jennifer U. Sung, Susan Vitale, and Peter A. Campochiaro, "Supplemental Oxygen Improves Diabetic Macular Edema: A Pilot Study," *Investigative Ophthalmology & Visual Science,* vol. 45, no. 2, p. 617–624, 2004.

[22] Ogura, Y., M. Takahashi, S. Ueno, and Y. Honda, "Hyperbaric Oxygen Treatment for Chronic Cystoid Macular Edema after Branch Retinal Vein Occlusion," *American Journal of Ophthalmology,* vol. 104, no. 3, pp. 301-302, 1987.

[23] "The effect of intensive treatment of diabetes on the development and progression of long-term complications in insulin-dependent diabetes mellitus," *New England Journal of Medicine,* vol. 329, pp. 977-986, 1993.

[24] Hardarson SH, Stefansson E, "Oxygen saturation in central retinal vein occlusion," *American Journal of Ophthalmology,* vol. 150, pp. 871-875, 2010.

[25] Huang D, Swanson E, Lin C, et al, "Optical coherence tomography," *Science,* vol. 254, pp. 1178-1181, 1991.

[26] Vivek J. Srinivasan, Sava Sakadžić, Iwona Gorczynska, Svetlana Ruvinskaya, Weicheng Wu, James G. Fujimoto, David A. Boas, "Quantitative cerebral blood flow with Optical Coherence Tomography," *Optics Express,* vol. 18, no. 3, pp. 2477-2494, 2010.

[27] Ji Yi, Wenzhong Liu, Siyu Chen, Vadim Backman, Nader Sheibani, Christine M. Sorenson, Amani A. Fawzi, Robert A. Linsenmeier, Hao F. Zhang, "Visible light optical coherence tomography measures retinal oxygen metabolic response to systemic oxygenation," *Light, science & applications,* vol. 4, no. 9, 2015.